Journal of MATERIALS RESEARCH

Article
DOI:10.1557/s43578-021-00462-5

EARLY CAREER SCHOLARS IN MATERIALS SCIENCE 2022

ANNUAL ISSUE

Ultrasonic additive manufacturing of nanocrystalline laminated composites

Austin A. Ward[1], Donovan N. Leonard[2], Hans-Henrik König[3], Greta Lindwall[3], Zachary C. Cordero[1,4,a)]

[1] Materials Science and NanoEngineering, Rice University, Houston, TX 77005, USA
[2] Manufacturing Sciences Division, Oak Ridge National Laboratory, Oak Ridge, TN 37831, USA
[3] Materials Science and Engineering, KTH Royal Institute of Technology, Brinellvägen 23, 100 44 Stockholm, Sweden
[4] Aeronautics and Astronautics, MIT, Cambridge, MA 02139, USA
[a)] Address all correspondence to this author. e-mail: zcordero@mit.edu

Received: 26 May 2021; accepted: 29 November 2021; published online: 8 January 2022

Ultrasonic additive manufacturing has been used to fabricate laminated composites of commercially pure aluminum and a nanocrystalline nickel–cobalt (nc-NiCo) alloy. The nc-NiCo alloy would not weld to itself but readily welded to aluminum. Thus, by alternating between foils of nc-NiCo and Al, we achieved multi-material laminates with strong interlayer bonding. Electron microscopy showed that the nanoscale grain structure of the nc-NiCo was preserved during deposition and that the nc-NiCo/Al weld interface was decorated with comminuted surface oxides as well as Al–Ni–Co intermetallics. These findings are considered in light of process models of junction growth, interdiffusion, and grain growth, which together reveal how the different pressure- and temperature dependences of these phenomena give rise to a range of processing conditions that maximize bonding while minimizing coarsening and intermetallic formation. This analysis quantitatively demonstrates that using a soft, low melting point interlayer material decouples junction growth at the weld interface from grain growth in the nc-NiCo, expanding the range of optimal processing conditions.

Zachary C. Cordero

Zachary C. Cordero is the Boeing Assistant Professor of Aeronautics and Astronautics at Massachusetts Institute of Technology (MIT), where he develops materials technologies for emerging spaceflight applications. His current research is focused on the design, processing, and performance of novel materials tailored to withstand the extreme operating conditions in reusable liquid-propellant rocket engines. To this end he is investigating the mechanisms of metal ignition in high-pressure, high-temperature oxygen environments, such as those encountered in SpaceX's Raptor and Blue Origin's BE-4 engines; developing physics-based material indices to guide material selection and design for ox-rich turbomachinery; developing a quantitative framework to predict under what conditions ox-compatible coatings will fail; and designing novel superalloys which are intrinsically ignition-resistant and can be formed into complex net-shapes using melt-based additive manufacturing techniques. Prior to joining the MIT faculty, Cordero was a professor of Materials Science at Rice University and prior to that a postdoctoral fellow at the Manufacturing Demonstration Facility at Oak Ridge National Laboratory. He is a recipient of young investigator awards from Air Force Office of Scientific Research and Army Research Office. He received an S.B. in Physics and Ph.D. in Materials Science and Engineering from MIT.

List of symbols

A_n	Nominal contact area (m^2)
A_r	Real contact area (m^2)
b	Half-width of sonotrode contact area (m)
c	Concentration (m^{-3})
D^{GB}	Grain boundary interdiffusivity (m^2/s)
D^{L}	Lattice interdiffusivity (m^2/s)
D_0^{GB}	Grain boundary interdiffusivity prefactor (m^2/s)
D_0^{L}	Lattice interdiffusivity prefactor (m^2/s)
d	Grain size (m)
d_s	Sonotrode diameter (m)
δ	Grain boundary width (m)
E	Elastic modulus (GPa)
$\dot{\varepsilon}$	Strain rate (s^{-1})
F	Normal load (N)
H	Hardness (MPa)
κ	Thermal diffusivity (m^2/s)
K	Thermal conductivity (W/m K)
k_b	Boltzmann constant (eV/K)
l	Heat diffusion distance (m)
L	Mass interdiffusion distance (m)
λ	Sonotrode oscillation amplitude (m)
M_0	Grain boundary mobility prefactor (m^3/s)
μ	Friction coefficient (-)
n	Grain growth exponent (-)
ν	Poisson's ratio (-)
q	Frictional heat flux (W/m^2)
Q_G	Activation energy for grain growth (eV)
Q^{GB}	Activation energy for grain boundary interdiffusion (eV)
Q^{L}	Activation energy for lattice interdiffusion (eV)
ρC_p	Volumetric heat capacity (J/m^3 K)
σ	Normal stress (MPa)
t	Time (s)
T_0	Build-plate temperature (K)
T	Temperature (K)
T_m	Melting point (K)
v	Sonotrode travel velocity (m/s)
f	Sonotrode oscillation frequency (s^{-1})
w	Sonotrode width (m)
χ	Weighting factor (–)

Introduction

Ultrasonic additive manufacturing (UAM) is a hybrid additive manufacturing technique that uses ultrasonic welding to deposit foil feedstock, then CNC machining to selectively remove excess material. During the deposition process, a cylindrical sonotrode rolls across the build envelope while it compresses the feedstock and vibrates transverse to its travel direction. The mechanical action of the sonotrode disrupts oxides and plastically deforms surface asperities at the weld interface, facilitating junction growth and metallurgical bonding [1]. Asperity deformation underneath the rolling sonotrode is promoted by frictional heating at the weld interface, which results in homologous temperatures in the range 0.4–0.8 [2]. Importantly, the thermal excursion during UAM is brief, making it an attractive approach for fabricating net-shaped components from thermally unstable materials [2–4]. Indeed, UAM has successfully densified Ni-base and Fe-base metallic glasses without disturbing their amorphous structure [5–7].

Nanocrystalline alloys are an important class of thermally unstable materials that, in theory, are ideal candidates for UAM because they can be economically produced as foils. However, a key challenge for UAM of nanocrystalline alloys is that their high hardness can inhibit asperity deformation and attendant interlayer bonding. In other high hardness materials systems (e.g., 316L [8], Ta [9], Ti [10, 11]) issues with weldability have been overcome by placing a soft constituent (e.g., Al foil) between layers of the harder constituent. The interlayer facilitates bonding by flowing around asperities on the harder constituent. Still, even with soft interlayers, junction growth requires some frictional heating which can activate structural evolution processes such as grain growth and, in multi-material laminates, intermetallic formation. These structural evolution processes are undesirable: grain growth leads to softening, and intermetallics can result in embrittlement. Thus, there are tradeoffs between junction growth, grain growth in the nanocrystalline constituent, and intermetallic formation which motivate the search for optimal processing conditions (e.g., sonotrode travel velocity, oscillation amplitude, normal load) that simultaneously maximize junction growth and suppress structural evolution.

In this paper, we investigate UAM of laminated composites of an ultrahigh strength nanocrystalline (nc) NiCo alloy and a commercial purity Al interlayer. We begin by assessing the processing and structure of nc-NiCo/Al laminated composites, focusing specifically on the effects of frictional heating on junction growth, grain growth, and intermetallic formation at the nc-NiCo/Al heterophase interfaces. Next, we use our experimental results to validate process models of these structural evolution phenomena. By integrating these models into a single framework for predicting the structure of heterophase interfaces in multi-material laminated composites fabricated via UAM, we determine processing conditions that maximize weld strength while minimizing coarsening and interdiffusion. This analysis suggests approaches for UAM of thermally unstable materials and for selecting interlayer materials that optimize mechanical properties and performance.

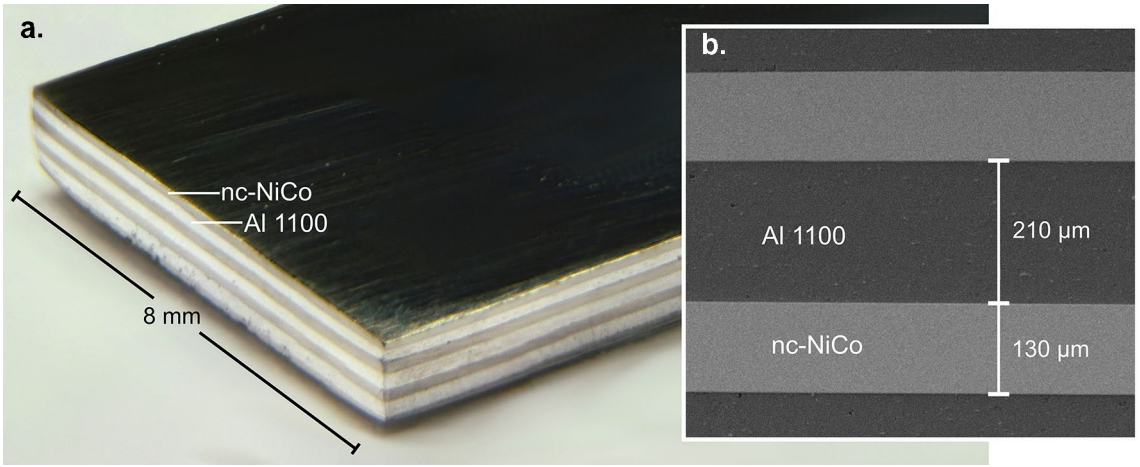

Figure 1: (a) Optical macrograph and (b) SEM micrograph of a nc-NiCo/Al laminate.

Experimental results and discussion

UAM of nc-NiCo/Al laminated composites

We determined UAM parameters for consolidating the nc-NiCo feedstock by independently varying the normal load (F), oscillation amplitude (λ), sonotrode velocity (v), and build-plate temperature (T_0) over the following ranges: $F = 7–10$ kN; λ = 16–23 μm; $v = 11–42$ mm/s; $T_0 = 339–394$ K. In initial tests, we welded nc-NiCo to itself and assessed weld quality through manual lap shear tests and peel tests. These attempts to print monolithic nc-NiCo builds were unsuccessful: Although some nc-NiCo welds were strong in shear, all had negligible tensile strength normal to the weld interface. Increasing F, increasing λ, and decreasing v to their respective limits—common strategies for improving interlayer bonding—resulted in fracture of the nc-NiCo sheet. In contrast, nc-NiCo sheets readily welded to commercially pure Al 1100 foil. Thus, by alternating between foils of Al 1100 and nc-NiCo, we fabricated nc-NiCo/Al laminates with robust interlayer bonding.

We used the following deposition procedure to prevent the Al from welding to the sonotrode. First, we simultaneously deposited a four-layer stack of foils in which two layers of nc-NiCo sandwiched a layer of Al foil while a 150 μm thick foil of a Ti alloy (ATI 425) separated the feedstock from the build-plate. Subsequently we deposited two layers at a time—one layer of Al foil and one of nc-NiCo sheet—with the layers arranged so that the nc-NiCo sheet was always closest to the sonotrode. To prevent tooling wear, we also placed an ATI 425 foil between the sonotrode and the nc-NiCo feedstock. A specialized vacuum fixture held the feedstock in place.

We found that the parameter set $F = 6$ kN, λ = 16 μm, $v = 42$ mm/s, and $T_0 = 333$ K produced well-bonded nc-NiCo/Al laminates. While this parameter set has a higher F and lower λ than is typically used to consolidate monolithic Al [13], Al alloys [1, 3, 14–16], and Al-base laminates [10, 17, 18], it resulted in a sonotrode power consumption of ~ 1.8 kW, in line with typical power values in UAM of Al alloys [14, 19].

Structural characterization

Figure 1 shows a nc-NiCo/Al laminate fabricated using the parameters reported above. The optical macrograph (Fig. 1a) and higher magnification SEM image (Fig. 1b) reveal flat, fully dense nc-NiCo/Al heterophase interfaces. These nc-NiCo/Al interfaces are distinct from the wavy weld interfaces commonly observed in UAM laminates [10, 17, 20, 21]. Such interfacial waviness results from the sonotrode indenting into the feedstock during the deposition process. This effect was suppressed in the present nc-NiCo/Al composites because of the ATI 425 spacer foil placed between the sonotrode and the feedstock.

The bright-field TEM micrograph of the nc-NiCo/Al interface shown in Fig. 2a reveals that the heterophase interface is flat even at the nanoscale, suggesting surface asperities on the rough Al foil flattened against the harder, smoother nc-NiCo material, which likely remained rigid and thus maintained its smooth initial surface profile. Figure 2a also highlights the distinct final structures of the Al and the nc-NiCo. In the Al foil, oxide dispersoids and intermetallic inclusions with dimensions on the order of several hundred nanometers decorate the grain boundaries. The mean grain size in the bulk is that of the as-received foils (1.5 μm) and decreases to ~ 50 nm in a region adjacent to the weld interface. Similar grain refinement observed in laminates of Al 3003 [21], steel [22, 23], and Cu [20] has been attributed to dynamic recrystallization processes, in which dislocations accumulate to form low-angle grain boundaries, which then coalesce into high-angle grain boundaries [23]. Interestingly, the thickness of this nanostructured region, 250 nm, is similar to the root-mean-square roughness of the Al feedstock,

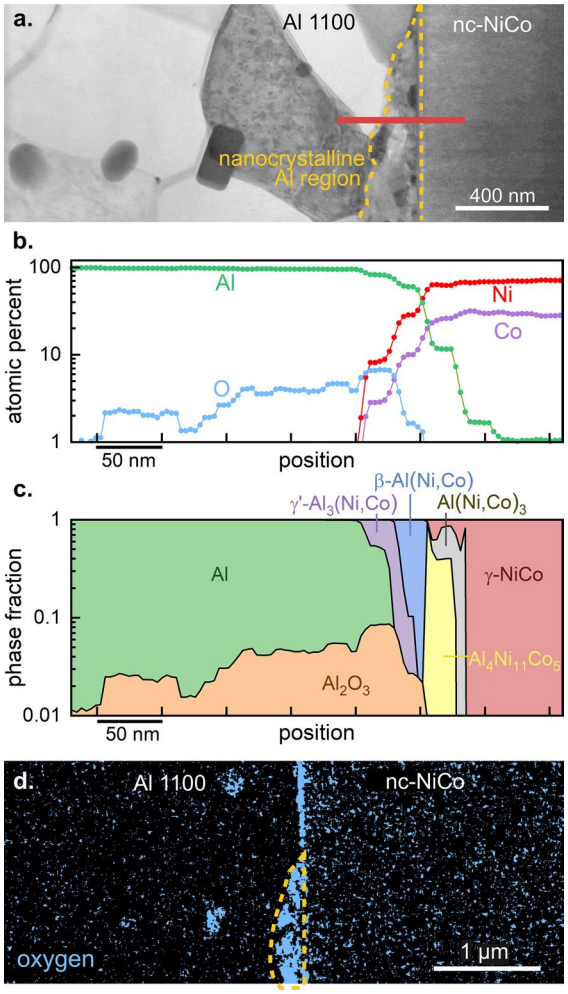

Figure 2: (a) Bright-field TEM image of a nc-NiCo/Al heterophase interface. (b) Composition as a function of position across the heterophase interface, as determined by STEM-EDS along the path indicated by the red line in (a). (c) Predicted equilibrium phase fractions as a function of position across a nc-NiCo/Al heterophase interface. Calculated at 800 K using Thermo-Calc software with the TCNI8 Ni-based superalloys database and the composition data shown in (b). (d) STEM-EDS chemical map of oxygen content showing high oxide concentration along the heterophase interface.

375 nm, suggesting the nanostructured region comprises flattened, severely deformed surface asperities.

In contrast with the Al foil, the nc-NiCo material has a grain structure that is uniform through the foil thickness. Figure 3a and b compare high-resolution TEM micrographs and selected-area electron diffraction (SAED) patterns taken from the virgin nc-NiCo feedstock and the as-deposited nc-NiCo, roughly 4 μm from the nc-NiCo/Al interface. The two materials are nearly indistinguishable. Both materials contain elongated grains, as are commonly observed in electrodeposited metals. The Debye rings in the diffraction patterns of the virgin and the as-deposited materials are all indexed to a face-centered cubic solid solution phase with the lattice parameter 3.535 Å, meaning the deposition process did not affect solute distribution several microns from the weld interface. Finally, quantitative stereological measurements of the grain size, summarized in Fig. 3c, show that the cumulative grain size distributions before and after ultrasonic welding are almost identical, with only a slight increase in mean grain size from 15 ± 1 nm to 18 ± 1 nm.

Although ultrasonic welding did not affect the structure in the bulk of the nc-NiCo material, there was evidence of nanoscale compositional changes in the immediate vicinity of the weld interface. Figure 2b, for example, presents results of a STEM-EDS line scan across the nc-NiCo/Al interface, along the path indicated in Fig. 2a. These data reveal a ~ 100 nm thick interdiffusion layer, with several steps in the concentrations of Al, Ni, and Co that indicate the presence of discrete intermetallic layers, each roughly ~ 10 nm wide. We identified these phases using the Thermo-Calc software with the TCNI8 materials database [24] and assuming an interfacial temperature of 800 K, slightly below the peak interfacial temperature of 825 K, determined in Sect. 4.1. The predicted phases and their respective phase fractions are summarized in Fig. 2c, which shows a series of intermetallics separating the terminal Al and NiCo phases. Importantly, the γ' and β phases have high strength but are brittle [25, 26], and therefore might weaken the interface.

To our knowledge, the only other experimental observation of intermetallic formation in UAM is due to Sietins et al. [27], who characterized heterophase interfaces in Al/Cu laminates and found a 400 nm thick interdiffusion layer that comprised CuAl and $CuAl_2$. While other investigators have claimed that UAM can suppress intermetallic formation [10, 17, 18, 28], the present experimental results, those of Sietins et al. [27], and the interdiffusion model discussed in Sect. 4.4 suggest that thin intermetallic layers readily form in multi-material UAM.

Figure 2b also reveals a region of high oxygen content that extends ~ 250 nm into the Al foil. The Thermo-Calc results indicate that this oxygen is sequestered as Al_2O_3, which could have been present as a surface oxide on the Al feedstock, then dispersed and mechanically mixed with the underlying metallic aluminum during the extensive plastic deformation that accompanies ultrasonic welding. This view is supported by the STEM-EDS chemical map of oxygen shown in Fig. 2d, in which a region of high oxygen content decorating the heterophase interface overlaps with the nanostructured aluminum region linked to the extensively deformed surface asperities. Near the interface, the oxide is mostly confined to the aluminum side of the interface, presumably because the weak Al surface asperities flowed around the much stronger nc-NiCo surface asperities without deforming them. This residual interfacial oxide might inhibit metallurgical bonding and further weaken the weld.

Hardness measurements from a nanoindentation traverse across several layers of a nc-NiCo/Al laminate are presented in Fig. 4. The mean hardness values of the Al and nc-NiCo layers are respectively 670 ± 10 MPa and 7.3 ± 0.1 GPa, identical to the hardness values of the as-received feedstocks. Consistent with the lack of grain growth seen in the TEM images, the spatially

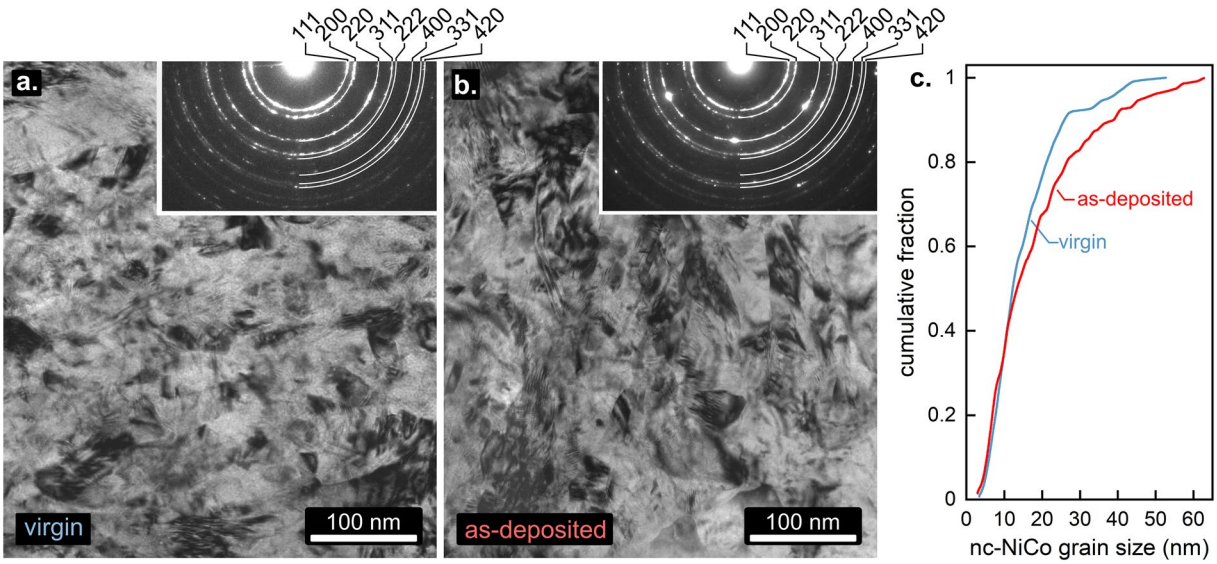

Figure 3: Bright-field TEM images of (a) virgin nc-NiCo feedstock and (b) as-deposited nc-NiCo roughly 4 μm from the weld interface. (c) Cumulative spherical-equivalent grain size distributions of the virgin and the as-deposited materials.

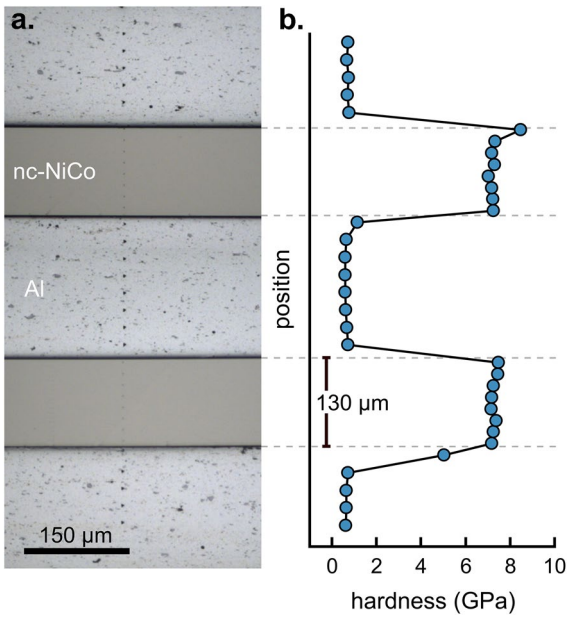

Figure 4: (a) Optical micrograph of an array of nanoindentation impressions across several layers of a nc-NiCo/Al composite and (b) corresponding hardness values.

uniform hardness measurements suggest that grain growth was negligible through the thickness of the nc-NiCo feedstock.

Structural evolution

The structural characterization results reveal a fully dense nc-NiCo/Al heterophase interface; minimal grain growth in the nc-NiCo; and a nanoscale interdiffusion layer decorated with several different Al–Ni–Co intermetallics. We next consider these results in light of recently developed process models of junction growth [2], grain growth [29], and interdiffusion [30] during UAM. Here we show how these models, which were developed and validated independently, can be integrated into a single framework for predicting the structure of the heterophase interfaces in UAM laminates. For the sake of completeness, we summarize these different models below, beginning with descriptions of contact stresses and frictional heating. We then use the models together to compute generalized UAM process diagrams which reveal important process-structure linkages, including benefits of using Al interlayers to consolidate nc-NiCo foils.

Temperature at the weld interfaces

During UAM, junction growth, grain growth, and interdiffusion all depend strongly on the temperature at the weld interface: thermal softening of surface asperities drives junction growth, while thermally activated grain boundary migration and mass transport drive grain growth and interdiffusion respectively. Thus, to model these different structural evolution processes, we first determine the temperature at the nc-NiCo/Al weld interface, following the experimentally validated procedure outlined in [2] with the modifications for multi-material UAM described in [30]. The key assumptions of this temperature model are: (i) the temperature field is steady-state in the moving frame of reference of the sonotrode; (ii) the heat flux injected into the weld interfaces is due entirely to friction; and (iii) roller-on-flat Hertzian contact mechanics describe the size of the contact patches and the normal stress distribution underneath the cylindrical sonotrode. Under this last

assumption, if the sonotrode travels in the x-direction, with the origin assigned to the sonotrode centerline, then the normal stress (σ) in the contact patch is

$$\sigma(x) = \frac{2F}{\pi w b}\sqrt{1-\left(\frac{x}{b}\right)^2}, \quad (1)$$

where w is the sonotrode width (2.54 cm), and b is the half-width of the contact patch in the sonotrode travel direction, given by

$$b = \sqrt{\frac{2Fd_s}{\pi w}\left(\frac{(1-\nu_{Al}^2)}{E_{Al}} + \frac{(1-\nu_{NiCo}^2)}{E_{NiCo}}\right)}. \quad (2)$$

Here, d_s is the sonotrode diameter (9.6 cm), and E and ν are the elastic modulus and Poisson's ratio of each foil material. The residence time of the sonotrode over a point on the weld interface is $t_r = 2b/v$, which ranges from 10 to several 100 ms.

Since nc-NiCo and Al foils are deposited simultaneously, there are two nc-NiCo/Al interfaces that experience gross slip and thus frictional heating during deposition. Considering the small separation between these interfaces (~ 100 μm) in comparison to the total heat diffusion distance (~ 1 cm), we approximate the total heat flux from these two interfaces as heating on a single plane at $z = 0$. The heat flux injected into this effective weld interface (q) is directly proportional to the normal stress:

$$q = \sqrt{2}\pi f \mu \sigma \lambda, \quad (3)$$

where μ is an effective friction coefficient and f is the sonotrode oscillation frequency (20 kHz). We note that the upper ATI 425 layer is considered an extension of the tooling and therefore frictional heating between the ATI 425 and nc-NiCo foils is taken to be negligible in comparison to the heat fluxes at the two active weld interfaces. To determine μ for the nc-NiCo/Al rubbing interface, we assume the power consumed by the sonotrode (P) is dissipated entirely as frictional work in the contact patches (i.e., $P = q$). Inserting the known process variables and the experimentally determined sonotrode power consumption (1.8 kW) into Eq. 3 gives $\mu = 0.21$. This friction coefficient is within the range typically observed during UAM of Al feedstock (0.05 to 0.64) [14, 15] and is consistent with the friction coefficient found to predict accurate interfacial temperatures during UAM of Al 3003-H18 and Al 6061-T6 [2]. We use this friction coefficient in the following calculations.

Table 1: Material properties.

Material	K (W/m·K)	ρC_p (J/cm^3·K)	κ (mm^2/s)	E (GPa)	ν (–)
AISI 1008	60.2[a]	3.78[a]	16	–	–
Al 1100-O	222[b]	2.45[b]	90	69[b]	0.33[b]
ATI 425	9.4[c]	2.34[b]	4	–	–
Ni	83[a]	3.97[d]	21	207[a]	0.31[a]
cp-Ti	19[e]	2.35[b]	8	108[b]	0.34[f]

[a]Harvey[34].
[b]ASM Handbook[33].
[c]ATI metals[35].
[d]Johnson and Cook[36].
[e]Powell[37].
[f]Welsch[38].

Inserting Eqs. 1–3, then convolving the position-dependent heat flux with the two-dimensional moving heat source solution due to Jaeger [31], we arrive at the following expression for the steady-state temperature in the moving frame of reference of the sonotrode:

$$T = T_0 + \frac{\sqrt{2}f\mu\lambda F}{\pi w b \overline{K}}\int_{-b}^{b}\sqrt{1-\left(\frac{x'}{b}\right)^2}\exp\left\{\frac{-v(x-x')}{2\overline{\kappa}}\right\}K_0\left\{\frac{v}{2\overline{\kappa}}\sqrt{(x-x')^2+z^2}\right\}dx', \quad (4)$$

where it is assumed that heat partitions evenly between the upper and lower surfaces at the weld interface and that the sonotrode is oscillating in the y-direction and applying a normal load in the z-direction. In Eq. 4, K_0 is the modified Bessel function of the second kind of order zero.

While the moving heat source solution due to Jaeger was originally developed for a homogeneous semi-infinite solid, we can extend his result to multi-material UAM by computing an effective thermal conductivity ($\overline{K}$), effective volumetric heat capacity ($\overline{\rho C_p}$), and effective thermal diffusivity ($\overline{\kappa} = \overline{K}/\overline{\rho C_p}$) to account for the different thermal properties of the various materials in the build. Approximating the materials as thermal insulators in series and considering only the lower half of the weld stack, we calculate $\overline{K}$ using an inverse rule-of-mixtures:

$$\frac{1}{\overline{K}} = \frac{\chi_{Al}}{K_{Al}} + \frac{\chi_{NiCo}}{K_{Ni}} + \frac{\chi_{ATI}}{K_{ATI}} + \frac{\chi_{build-plate}}{K_{build-plate}}, \quad (5)$$

where the subscripts refer to the different constituents and χ_i is a weighting factor discussed below. Following Ashby [32], we calculate $\overline{\rho C_p}$ using a rule-of-mixtures:

$$\overline{\rho C_p} = \chi_{Al}(\rho C_p)_{Al} + \chi_{NiCo}(\rho C_p)_{Ni} + \chi_{ATI}(\rho C_p)_{ATI} + \chi_{build-plate}(\rho C_p)_{build-plate}. \quad (6)$$

The mechanical and thermal properties of the constituents are summarized in Table 1, where the thermal properties of nc-NiCo are assumed to be the same as those of conventional microcrystalline Ni [33].

The weighting factor χ_i is the heat diffusion distance l_i into each constituent normalized by the sum total heat diffusion distance:

$$\chi_i = \frac{l_i}{l_{Al} + l_{NiCo} + l_{ATI} + l_{build-plate}}. \quad (7)$$

The time for heat to diffuse through each foil individually, estimated as ρ^2/κ, where ρ is the foil thickness, is on the order of 1 ms. Since this timescale is only a fraction of t_r, we set l_i for the Al, nc-NiCo, and ATI 425 layers to their respective foil thicknesses. The heat diffusion distance into the build-plate is estimated using $\sqrt{\kappa_{build-plate} t_r}$, giving $l_{build\text{-}plate}$ values between 0.02 and 2 mm.

Junction growth

Junction growth via plastic deformation at the weld interface is aided by (i) thermal softening of surface asperities due to frictional heating [2] and (ii) strain ratcheting due to yielding under the combined action of a normal pressure and a shear stress [39]. However, the normality condition which gives rise to strain ratcheting can break down at a sliding interface lubricated with surface contaminants or oxide overlayers [40]. Thus in the present calculations we only consider thermal softening effects.

When nominally flat but microscopically rough surfaces are pressed against each other, their real contact area (A_r) is a fraction of the nominal contact area (A_n). At a dissimilar metal interface, the ratio A_r/A_n, which corresponds to the linear weld density, equals the ratio of the normal contact pressure (σ) to the temperature-dependent surface hardness (H) of the weaker constituent [30],

$$\frac{A_r}{A_n} = \frac{\sigma}{H}. \quad (8)$$

Here, σ is given by Eq. 1, and H is computed for Al 1100 using a modified form of the Johnson–Cook equation:

$$H = 3A^* \left[C + D \ln\left(\frac{\dot{\varepsilon}}{\dot{\varepsilon}_0} \right)^p \right] \left[1 - \left(\frac{T - T_0}{T_m - T_0} \right)^m \right], \quad (9)$$

where $\dot{\varepsilon}$ is the nominal strain rate at the interface, which we estimate as 10^4 s^{-1} [2], and $A^* = 159$ MPa; $C = 0.46$; $D = 0.49$; $m = 0.51$; $p = 0.1$; $\dot{\varepsilon}_0 = 1$ s^{-1} [41]. Note that because the normal pressure and the temperature both vary with position under the sonotrode in UAM, the fractional contact area is also position-dependent. Figure 7 in [2] plots the steady-state fractional contact area under a moving sonotrode under several different processing conditions, showing how the fractional contact area increases monotonically from the leading edge to the trailing edge of the sonotrode, until reaching a maximum value that depends on material properties and processing conditions. Interfacial porosity is eliminated completely when the fractional contact area equals unity, or $\sigma = H$.

Grain growth

The physical mechanisms that drive grain structure evolution during UAM depend on the initial grain size of the feedstock and on distance from the weld interface. Elevated temperatures due to frictional heating will activate recrystallization and grain growth both in conventional microcrystalline materials and in nanocrystalline materials [29]. In addition, extensive plastic deformation in the immediate vicinity of the weld interface can influence grain structure, with different effects depending on initial grain size. In microcrystalline materials, plastic deformation causes grain refinement (cf. the Al foil in Fig. 3a) [20, 23]. By contrast, in nanocrystalline materials, plastic deformation can cause shear-coupled grain boundary migration and grain growth [42]. Such deformation-induced grain growth has been observed during low-temperature, severe plastic deformation processing of nanocrystalline metals [42] and is therefore expected at weld interfaces in UAM, where the cumulative plastic shear strain is of the order 10^4, far higher than the cumulative shear strains in equal channel angular extrusion [43–45] or high pressure torsion [46–48].

Modeling deformation-induced grain refinement or grain coarsening remains a major challenge, making it difficult to predict the grain size at the weld interface under most conditions. However, in the nc-NiCo/Al laminated composites of interest here, our structural characterization results show that plastic deformation at the weld interface is confined to the weaker Al foil. As a result, we can ignore deformation-induced coarsening in the nc-NiCo foil and estimate the nc-NiCo grain size (d) by integrating the classical grain growth law due to Hu and Rath [49] over the thermal cycle experienced during material deposition:

$$d^n = d_0^n + M_0 \int_0^t \frac{1}{T(t)} \exp[-Q_G/k_B T(t)] dt. \quad (10)$$

Here, d_0 is the initial grain size and k_B is the Boltzmann constant. n, M_0, and Q_G are material-dependent grain growth parameters [50]. Because these parameters have not been determined for nc-NiCo, the following analysis uses values for nominally pure nc-Ni [51]: $M_0 = 1.3 \times 10^{-11}$ m^3/s; $Q_G = 1.26$ eV; $n = 3$.

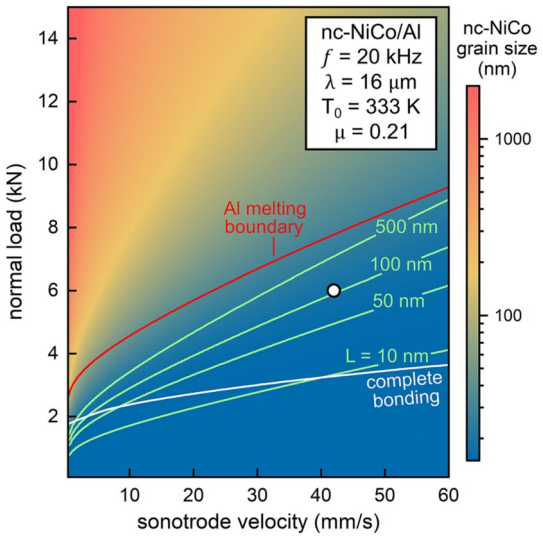

Figure 5: Process diagram for UAM of nc-NiCo/Al laminated composites, assuming $\lambda = 16$ μm; $T_0 = 333$ K; $f = 20$ kHz. Color map indicates predicted final grain size of NiCo material. Iso-contours of interdiffusion distance are shown in green. Processing conditions above the complete bonding contour give fully dense nc-NiCo/Al interfaces. Processing conditions above the aluminum melting contour have a peak interfacial temperature that exceeds the melting point of Al (925 K). The white circle corresponds to the experimental processing conditions.

Interdiffusion

Frictional heating also accelerates thermally activated interdiffusion across the weld interface. While several investigators have claimed that there is anomalously fast interdiffusion during ultrasonic welding and have attributed this effect to exotic physics (e.g., solute transport via dislocation motion [52], vacancy supersaturation due to extensive plastic deformation [53]), we recently showed that the extent of interdiffusion can be estimated accurately by combining the temperature field at the weld interface and the standard form of Fick's second law. Following our analysis in [30], the concentration (c) evolves according to

$$\frac{\partial c}{\partial t} = \overline{D}\frac{\partial^2 c}{\partial z^2} \tag{11}$$

where $\overline{D}$ is an interdiffusivity. $\overline{D}$ changes with time as the steady-state temperature profile translates across the region of interest. Because the thermal diffusivities of the feedstocks are much larger than their interdiffusivity, we can ignore the z dependence of the temperature field and just use the x-dependent interfacial temperature to compute $\overline{D}$.

For simplicity, we use an effective interdiffusivity to describe mass transport across the different phases at the nc-NiCo/Al interface, a common approximation in modeling interdiffusion [54]. Additionally, to account for short-circuit diffusion along grain boundaries in nc-NiCo, we use a volume average of the lattice interdiffusivity (D^{L}) and the grain boundary interdiffusivity (D^{GB}) [55]:

$$D = D^{\mathrm{L}} + (3\delta/d_0)D^{\mathrm{GB}} \tag{12}$$

where δ is the grain boundary width, assumed to be 0.6 nm [56]. D^{L} and D^{GB} are computed using

$$D^{\mathrm{L}} = D_0^{\mathrm{L}} \exp\left[-Q^{\mathrm{L}}/k_{\mathrm{B}}T\right]. \tag{13}$$

and

$$D^{\mathrm{GB}} = D_0^{\mathrm{GB}} \exp\left[-Q^{\mathrm{GB}}/k_{\mathrm{B}}T\right]. \tag{14}$$

Since the prefactors and activation energies in Eqs. 13 and 14 have not been determined for the Ni-Co-Al ternary, we instead use values for Ni–Al interdiffusion [56, 57]: $D_0^{\mathrm{L}} = 0.65$ cm^2/s; $D_0^{\mathrm{GB}} = 0.01$ cm^2/s; $Q^{\mathrm{L}} = 2.7$ eV; $Q^{\mathrm{GB}} = 1.2$ eV.

Process diagrams for UAM of laminated composites

Figure 5 is a UAM process diagram that shows the extent of junction growth, grain growth, and interdiffusion at heterophase interfaces in nc-NiCo/Al laminates. The diagram was computed using the expressions developed above, assuming the same preheat temperature (333 K), sonotrode oscillation frequency (20 kHz), and sonotrode oscillation amplitude (16 μm) as used in our UAM experiments. The axes of normal load and sonotrode travel velocity span typical ranges accessible with high-power UAM [58]. The color map corresponds to the final grain size of the nc-NiCo material at the weld interface. The iso-contours shown in green indicate processing conditions that yield a given interdiffusion distance (L), defined as the distance normal to the weld interface between Ni concentrations $c = 0.01$ and 0.99. The Al melting boundary, shown in red, indicates combinations of normal load and sonotrode travel velocity for which the peak interfacial temperature just reaches the melting point of aluminum ($T_{\mathrm{m}} = 933$ K). Lastly, the contour labeled complete welding indicates parameters for which $\sigma = H_{\mathrm{Al}}$, thus resulting in fully dense welds; combinations of normal load and sonotrode travel velocity that lie above this curve will also give fully dense welds but involve excessive heating of the feedstock.

In Fig. 5, the filled circle corresponds to the combination of normal load and sonotrode velocity that we determined through trial-and-error experimentation. These processing conditions result in a predicted mean contact pressure of 230 MPa, contact width of 1 mm, contact time of 20 ms, and peak interfacial temperature of 825 K. This peak interfacial temperature is ~ 30 K higher than that predicted for UAM of monolithic aluminum processed under identical conditions because the lower thermal diffusivity of the nc-NiCo foil retains heat near the weld interface. The experimental processing conditions lie between the melting boundary and the complete welding boundary, consistent with our observations of a fully dense nc-NiCo/Al interface,

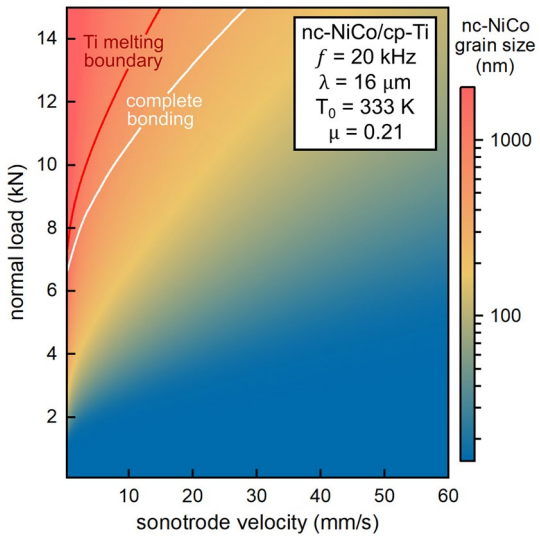

Figure 6: Process diagram for the consolidation of nc-NiCo/cp-Ti laminates using the same oscillation amplitude, oscillation frequency, and ambient temperature as used in Fig. 5. Processing conditions above the Ti melting boundary lead to peak interfacial temperatures higher than the melting point of cp-Ti (1941 K).

free of features characteristic of melting. The predicted nc-NiCo grain size and interdiffusion distance are 23 nm and 115 nm, respectively, in reasonable agreement with the experimental values of 18 nm and 105 nm. The overall good agreement between the interfacial structure determined through experiment and that predicted by the process models give confidence that this computational framework can be used to identify optimal processing conditions, eliminating some of the trial-and-error in UAM of new materials and material combinations.

The processing conditions in the region bounded by the Al melting contour and the complete welding contour give fully dense laminates without melting of Al. Within this window, grain growth in nc-NiCo is minimal. Additionally, following the complete welding contour to the right shows that simultaneously increasing sonotrode travel velocity and normal load should help minimize coarsening and interdiffusion. The different forms of the grain growth, junction growth, and interdiffusion contours highlight the disparate interfacial temperature- and contact pressure dependences of these structural evolution processes. In particular, Fig. 5 shows how the presence of the aluminum interlayer decouples the junction growth and grain growth behaviors, since the mechanical properties of the soft Al interlayer determine the extent of junction growth while the physical properties of nc-NiCo determine the extent of coarsening.

To further illustrate the effects of interlayer properties on structural evolution, Fig. 6 shows another UAM process diagram for laminated composites of nc-NiCo and 210 μm thick sheets of commercially pure Ti (cp-Ti). This diagram was calculated using the Johnson–Cook parameters of cp-Ti ($A^* = 1289$ MPa; $C = 1$; $D = 0.019$; $m = 0.66$; $p = 1$; $\dot{\varepsilon}_0 = 1$ [59]) and the thermal properties of cp-Ti listed in Table 1; all other parameters are the same as in Fig. 5. Again, the processing conditions in the region bounded by the Ti melting contour and the complete welding contour give fully dense laminates without melting either constituent. The location of this processing window is shifted to higher normal loads and lower sonotrode velocities as compared to the processing window in Fig. 5. Additionally, the processing window in Fig. 6 is much narrower and the extent of grain growth much greater than in Fig. 5. Specifically, the predicted final nc-NiCo grain sizes on the complete bonding contour for nc-NiCo/Ti laminates range from 295 to 660 nm, compared to nc-NiCo grain sizes of 15 to 40 nm for completely bonded nc-NiCo/Al laminates. These changes are due to the higher melting point and strength of Ti versus Al, which mean higher peak interfacial temperatures are required to achieve complete bonding in nc-NiCo/Ti composites. Comparing Figs. 5 and 6 clearly demonstrates the benefits of using soft, low melting point interlayers to minimize the thermal excursion at the weld interface during UAM of laminates with a thermally unstable constituent.

Conclusions

We have used ultrasonic additive manufacturing (UAM) to fabricate multi-material laminates from nanocrystalline nc-NiCo sheets and commercially pure Al foil. Composites fabricated with optimized parameters had smooth, fully dense weld interfaces. TEM investigations on these composites revealed that:

- The nanoscale grain structure of the nc-NiCo feedstock was preserved during consolidation.
- The Al adjacent to the weld interface was nanostructured and contained a dispersion of nano-oxides, indicating that the soft, oxide-covered Al surface asperities experienced severe plastic deformation as they flattened against the harder, smoother nc-NiCo surface.
- The constituents diffused into each other, forming several different Al–Ni–Co intermetallics, confirming that intermetallic layers on the order of 100 nm can grow at the weld interface during ultrasonic additive manufacturing despite the brief thermal excursion.

These experimental observations were in quantitative agreement with process models of grain growth, junction growth, and interdiffusion. By combining these models into a single framework, we showed how the different temperature- and contact pressure dependences of grain growth, junction growth, and interdiffusion give rise to a range of processing conditions that simultaneously preserve the structure of nanocrystalline feedstock, achieve fully dense interfaces, and

minimize interdiffusion. Process diagrams computed for different material combinations show how judicious selection of the interlayer material can expand this process window, by decoupling junction growth (which depends on the mechanical properties of the interlayer material) from grain growth (which depends on the physical properties of the nanocrystalline constituent). These calculations quantitatively demonstrate the benefits of using soft, low melting point interlayers to consolidate nanocrystalline foils.

The process modeling framework introduced here can accurately predict the structure of heterophase interfaces in UAM laminates; however, going one step further to predict interlaminar strength remains a significant challenge. The underlying reason is that interlaminar strength depends not only on the extent of junction growth, but also on the presence of interfacial phases, such as oxides and intermetallics, whose effects on mechanical properties are poorly understood. Brittle intermetallics, like those found at the nc-NiCo/Al interface, are generally expected to degrade interfacial strength; however, thick intermetallic layers formed during post-processing heat treatments have been found to strengthen the interfaces in Al/Ti and Al/Cu laminates fabricated using UAM [17, 60]. Interfacial oxides, like those seen in Fig. 3b, c, prevent the growth of strong metallurgical junctions, but estimating their effect on interlaminar strength is difficult, in part because explanations of oxide breakdown are qualitative and cannot predict the final spatial distribution of the oxide at the weld interface. Future work should address these gaps in understanding, with a view toward quantitatively assessing how interfacial phases, such as the oxides and intermetallics found at the nc-NiCo/Al interface, degrade the interlaminar strength of UAM laminates.

Materials and methods

A Fabrisonic SonicLayer 4000 UAM machine was used to print laminated composites from Al 1100-O foils and electrodeposited sheets of a nanocrystalline Ni-28Co, at.% alloy (nc-NiCo). The UAM build-plate material was AISI 1008, and the sonotrode material was 350 maraging steel. The sonotrode had a diameter of 9.6 cm and width of 2.54 cm. The Al foil feedstock had a nanoindentation hardness of 660 MPa, thickness of 210 μm, and an initial grain size on the scale of microns. Note that the initial grain size near the surface of the Al foil was also on the scale of microns. The nc-NiCo foil (Integran Technologies) had an initial nanoindentation hardness of 7.2 GPa, thickness of 130 μm, and initial grain size of 15 nm. The nc-NiCo alloy comprised a single-phase FCC solid solution of Ni and Co, with S and C impurity concentrations on the order of several hundred ppm [12]. The root-mean-square surface roughness values of the nc-NiCo and the Al foils were 15 nm and 375 nm, respectively, as determined using optical profilometry. The initial nanoindentation hardness values of the as-received Al and nc-NiCo foils were 660 ± 10 MPa and 7.3 ± 0.1 GPa, respectively.

Electron microscopy was used to characterize the structures of the nc-NiCo feedstock and the nc-NiCo/Al laminated composites. The laminated composites were mounted in epoxy, polished, and imaged using a FEI Quanta 400 scanning electron microscope (SEM) operated at 20 kV. Transmission electron microscopy (TEM) samples were extracted from the nc-NiCo and the nc-NiCo/Al materials using the focused ion beam (FIB) lift-out technique, then imaged in a FEI Talos F200X operated at 200 kV and fitted with a SuperX EDS system.

Nanoindentation testing was used to assess the hardness of each constituent in the as-deposited composites. These experiments were performed on a Hysitron TI 980 Triboindenter, operated in load control with a Berkovich indenter, using peak loads of 7.2 mN on Al and 11 mN on nc-NiCo.

Acknowledgments

We are grateful to Dr. Adam Hehr and Mr. Mark Norfolk of Fabrisonic for performing the UAM experiments. G.L. and H-H.K. acknowledge support from the VINNOVA agency via the LIGHTer academy. Z.C.C acknowledges financial support provided by the Army Research Office under Award No. W911NF-17-1-0342.

Data availability

The data that support the findings of this study are available from Z.C.C. upon reasonable request.

Declarations

Conflict of interest The authors declare that they have no known competing financial interests or personal relationships that could have appeared to influence the work reported in this paper.

Open Access

References

1. Y. Yang, G.D. Janaki Ram, B.E. Stucker, Bond formation and fiber embedment during ultrasonic consolidation. J. Mater. Process. Technol. **209**(10), 4915 (2009)
2. A.A. Ward, Y. Zhang, Z.C. Cordero, Junction growth in ultrasonic spot welding and ultrasonic additive manufacturing. Acta Mater. **158**, 393 (2018)
3. M.R. Sriraman, M. Gonser, D. Foster, H.T. Fujii, S.S. Babu, M. Bloss, Thermal transients during processing of 3003 Al-H18 multilayer build by very high-power ultrasonic additive manufacturing. Metall. Trans. B. **43**(1), 133 (2012)
4. M.R. Sriraman, M. Gonser, H.T. Fujii, S.S. Babu, M. Bloss, Thermal transients during processing of materials by very high power ultrasonic additive manufacturing. J. Mater. Proc. Technol. **211**(10), 1650 (2011)
5. W. Wu, J. Jiang, G. Li, J.Y.H. Fuh, H. Jiang, P. Gou, L. Zhang, W. Liu, J. Zhao, Ultrasonic additive manufacturing of bulk Ni-based metallic glass. J. Non-Cryst. Solids **506**, 1 (2019)
6. Y. Wang, Q. Yang, X. Liu, Y. Liu, B. Liu, R. Misra, H. Xu, P. Bai, Microstructure and mechanical properties of amorphous strip/aluminum laminated composites fabricated by ultrasonic additive consolidation. Mater. Sci. Eng. A **749**, 74 (2019)
7. Z. Li, S. Wu, X. Huang, N. Li, Versatile fabrication of bulk metallic glass composites reinforced by dissimilar secondary phase. Mater. Sci. Eng. A **791**, 139643 (2020)
8. S. Kumar, Development of functionally graded materials by ultrasonic consolidation. J. Manuf. Sci. Technol. **3**(1), 85 (2010)
9. J. Obielodan, A. Ceylan, L. Murr, B. Stucker, Multi-material bonding in ultrasonic consolidation. Rapid Prototyp. J. **16**(3), 180 (2010)
10. N. Sridharan, P. Wolcott, M. Dapino, S.S. Babu, Microstructure and texture evolution in aluminum and commercially pure titanium dissimilar welds fabricated using ultrasonic additive manufacturing. Scr. Mater. **117**, 1 (2016)
11. C. Hopkins, M. Dapino, S. Fernandez, Statistical characterization of ultrasonic additive manufacturing Ti/Al composites. J. Eng. Mater. Technol. **132**(4), 041006 (2010)
12. G. Hibbard, K. Aust, U. Erb, Thermal stability of electrodeposited nanocrystalline Ni–Co alloys. Mater. Sci. Eng. A **433**(1–2), 195 (2006)
13. G.S. Kelly, M.S. Just, S.G. Advani, J.W. Gillespie, Energy and bond strength development during ultrasonic consolidation. J. Mater. Process. Technol. **214**(8), 1665 (2014)
14. D. Yi, S. Zhang, H. Zhang, L. Zheng, M. Norfolk, Power consumption and friction coefficient in the ultrasonic consolidation of aluminium alloys. Mater. Sci. Technol. **33**(6), 744 (2016)
15. S. Koellhoffer, J.W. Gillespie, S.G. Advani, T.A. Bogetti, Role of friction on the thermal development in ultrasonically consolidated aluminum foils and composites. J. Mater. Process. Technol. **211**(11), 1864 (2011)
16. J. Obielodan, G. Ram, B. Stucker, D. Taggart, Minimizing defects between adjacent foils in ultrasonically consolidated parts. J. Eng. Mater. Technol. **132**(1), 011006 (2010)
17. P. Wolcott, N. Sridharan, S.S. Babu, A. Miriyev, N. Frage, M.J. Dapino, Characterisation of Al–Ti dissimilar material joints fabricated using ultrasonic additive manufacturing. Sci. Technol. Weld. Join. **21**(2), 114 (2016)
18. J. Obielodan, B. Stucker, E. Martinez, J. Martinez, D. Hernandez, D. Ramirez, L. Murr, Optimization of the shear strengths of ultrasonically consolidated Ti/Al 3003 dual-material structures. J. Mater. Process. Technol. **211**(6), 988 (2011)
19. A. Hehr, P.J. Wolcott, M.J. Dapino, Effect of weld power and build compliance on ultrasonic consolidation. Rapid Prototyp. J. **22**, 377 (2016)
20. M.R. Sriraman, S.S. Babu, M. Short, Bonding characteristics during very high power ultrasonic additive manufacturing of copper. Scr. Mater. **62**(8), 560 (2010)
21. R.R. Dehoff, S.S. Babu, Characterization of interfacial microstructures in 3003 aluminum alloy blocks fabricated by ultrasonic additive manufacturing. Acta Mater. **58**(13), 4305 (2010)
22. A. Levy, A. Miriyev, N. Sridharan, T. Han, E. Tuval, S.S. Babu, M.J. Dapino, N. Frage, Ultrasonic additive manufacturing of steel: method, post-processing treatments and properties. J. Mater. Process. Technol. **256**, 183 (2018)
23. N. Sridharan, M. Norfolk, S.S. Babu, Characterization of steel-Ta dissimilar metal builds made using very high power ultrasonic additive manufacturing (VHP-UAM). Metall. Mater. Trans A. **47**(5), 2517 (2016)
24. J.-O. Andersson, T. Helander, L. Höglund, P. Shi, B. Sundman, Thermo-Calc & DICTRA, computational tools for materials science. Calphad **26**(2), 273 (2002)
25. L. Sheng, W. Zhang, J. Guo, Z. Wang, V. Ovcharenko, L. Zhou, H. Ye, Microstructure and mechanical properties of Ni_3Al fabricated by thermal explosion and hot extrusion. Intermetallics **17**(7), 572 (2009)
26. D. Miracle, Overview No. 104 The physical and mechanical properties of NiAl. Acta Metall. Mater. **41**(3), 649 (1993)
27. J.M. Sietins, J.W. Gillespie, S.G. Advani, Transmission electron microscopy of an ultrasonically consolidated copper–aluminum interface. J. Mater. Res. **29**(17), 1970 (2014)
28. R. Hahnlen, M.J. Dapino, NiTi–Al interface strength in ultrasonic additive manufacturing composites. Compos. B Eng. **59**, 101 (2014)
29. A.A. Ward, M.R. French, D.N. Leonard, Z.C. Cordero, Grain growth during ultrasonic welding of nanocrystalline alloys. J. Mater. Process. Technol. **254**, 373 (2018)

30. A.A. Ward, Z.C. Cordero, Junction growth and interdiffusion during ultrasonic additive manufacturing of multi-material laminates. Scripta Mater. **177**, 101 (2020)
31. J. Jaeger, Moving heat sources and friction temperature. Proc. R. Soc. NSW **76**, 203 (1942)
32. M.F. Ashby, Criteria for selecting the components of composites. Acta Metall. Mater. **41**(5), 1313 (1993)
33. ASM Handbook, *Nonferrous Alloys and Special-Purpose Materials*, vol. 2 (ASM International, Geauga, 1990)
34. P. Harvey, *Engineering Properties of Steel* (ASM International, Geauga, 1982)
35. ATI 425 Technical Data Sheet Allegheny Technologies Inc
36. G.R. Johnson, W.H. Cook: A constitutive model and data for metals subjected to large strains, high strain rates and high temperatures, in Proceedings of the 7th International Symposium on Ballistics (**21**, 1983), p. 541
37. R. Powell, R. Tye, The thermal and electrical conductivity of titanium and its alloys. J Less COMMON Met. **3**(3), 226 (1961)
38. G. Welsch, R. Boyer, E.W. Collings, *Materials Properties Handbook: Titanium Alloys* (ASM International, Geauga, 1993)
39. G.S. Daehn, *Plastic Consolidation of Metal Matrix Composites by Pressure Cycling, in 60 Excellent Inventions in Metal Forming* (Springer, New York, 2015), p. 415
40. D. Tabor, Junction growth in metallic friction: the role of combined stresses and surface contamination. Proc. R. Soc. Lond A **251**, 378 (1959)
41. Q. Mao, *Understanding the Bonding Process of Ultrasonic Additive Manufacturing* (Clemson University, Clemson, 2017)
42. X. Liao, A. Kilmametov, R. Valiev, H. Gao, X. Li, A. Mukherjee, J. Bingert, Y. Zhu, High-pressure torsion-induced grain growth in electrodeposited nanocrystalline Ni. Appl. Phys. Lett. **88**(2), 021909 (2006)
43. A. Mishra, B. Kad, F. Gregori, M. Meyers, Microstructural evolution in copper subjected to severe plastic deformation: experiments and analysis. Acta Mater. **55**(1), 13 (2007)
44. H. Mughrabi, H. Höppel, M. Kautz, Fatigue and microstructure of ultrafine-grained metals produced by severe plastic deformation. Scripta Mater. **51**(8), 807 (2004)
45. T. Aida, K. Matsuki, Z. Horita, T.G. Langdon, Estimating the equivalent strain in equal-channel angular pressing. Scripta Mater. **44**(4), 575 (2001)
46. A. Korznikov, G. Tram, O. Dimitrov, G. Korznikova, S. Idrisova, Z. Pakiela, The mechanism of nanocrystalline structure formation in Ni_3Al during severe plastic deformation. Acta Mater. **49**(4), 663 (2001)
47. S. Ni, Y. Wang, X. Liao, S. Alhajeri, H. Li, Y. Zhao, E. Lavernia, S. Ringer, T. Langdon, Y. Zhu, Strain hardening and softening in a nanocrystalline Ni–Fe alloy induced by severe plastic deformation. Mater. Sci. Eng. A **528**(9), 3398 (2011)
48. Y. Estrin, A. Vinogradov, Extreme grain refinement by severe plastic deformation: a wealth of challenging science. Acta Mater. **61**(3), 782 (2013)
49. H. Hu, B.B. Rath, On the time exponent in isothermal grain growth. Metall. Mater. Trans. B **1**(11), 3181 (1970)
50. J.E. Burke, D. Turnbull, Recrystallization and grain growth. Prog. Met. Phys. **3**, 220 (1952)
51. M. Thuvander, M. Abraham, A. Cerezo, G. Smith, Thermal stability of electrodeposited nanocrystalline nickel and iron–nickel alloys. Mater. Sci. Technol. **17**(8), 961 (2001)
52. J. Yang, B. Cao, Investigation of resistance heat assisted ultrasonic welding of 6061 aluminum alloys to pure copper. Mater. Des. **74**, 19 (2015)
53. I.E. Gunduz, T. Ando, E. Shattuck, P.Y. Wong, C.C. Doumanidis, Enhanced diffusion and phase transformations during ultrasonic welding of zinc and aluminum. Scr. Mater. **52**(9), 939 (2005)
54. S. Bader, W. Gust, H. Hieber, Rapid formation of intermetallic compounds interdiffusion in the Cu-Sn and Ni-Sn systems. Acta Metall. Mater. **43**(1), 329 (1995)
55. E. Hart, On the role of dislocations in bulk diffusion. Acta Metall. **5**(10), 597 (1957)
56. K. Smidoda, C. Gottschalk, H. Gleiter, Grain boundary diffusion in migrating boundaries. Met. Sci. **13**(3–4), 146 (1979)
57. R. Swalin, A. Martin, Solute diffusion in nickel-base substitutional solid solutions. J. Met. **8**, 567 (1956)
58. H.T. Fujii, M. Sriraman, S. Babu, Quantitative evaluation of bulk and interface microstructures in Al-3003 alloy builds made by very high power ultrasonic additive manufacturing. Metall. Mater. Trans. A **42**(13), 4045 (2011)
59. G. Bae, S. Kumar, S. Yoon, K. Kang, H. Na, H.-J. Kim, C. Lee, Bonding features and associated mechanisms in kinetic sprayed titanium coatings. Acta Mater. **57**(19), 5654 (2009)
60. A.G. Truog, *Bond Improvement of Al/Cu Joints Created by Very High Power Ultrasonic Additive Manufacturing* (The Ohio State University, Ohio, 2012)